Wind Turbine Team at Virginia Tech
Technical Design Written Report
2022 U.S. Department of Energy Collegiate Wind Competition

Virginia Tech
Blacksburg, Virginia, WindTurbineTeamVT@vt.edu
Twitter/Instagram/Facebook: @WindTurbineTeamVT

Team Leads
Hayley Capilitan (Project Manager) | **Emily Philpott** (Project Manager)
Emily Sellards & Laura Dawson (Blades)
Garrett Kemmerly & Om Shah (Mechanical Systems) | **Kai Kato** (Systems Integration)
Olivia Moldoveanu (Power Systems and Controls)

Advisors
Dr. Matthew Kuester (Principal Investigator, Department of Aerospace Engineering)
Dr. Arthur Ball (Assistant Investigator, Department of Electrical and Computer Engineering)
Members: 44 (9 majors), Advisors: 2

Table of Contents

Executive Summary

The goal of the Wind Turbine Team at Virginia Tech this year was to focus on a specific design objective: to innovate system components to optimize assembly, operation, and performance of the entire prototype. This objective was inspired by the innovative offshore foundation challenge new to this year's competition. With many experienced seniors and younger returning members, focus was shifted to implementing advanced concepts and thorough engineering analyses to generate a reliable, durable wind turbine for the 2022 Collegiate Wind Competition.

Figure 1. Full Turbine Assembly

As a result of the offshore foundation in this year's design, the team adopted a ground-up approach in analyzing turbine subsystems. Major upgrades to this year's assembly include: a fully redesigned hub and pitch control system, electronic universally controllable load, and the foundation itself. Each of these components was critically compared against alternative designs; the iterative process followed to create the final product is detailed within this report. While considering solutions, emphasis was placed on minimizing the complexity of the full assembly by reducing the number of subsystems required to complete each competition task. For example, the team was successfully able to remove redundant subsystems, such as the mechanical brake, due to the efficiency of redesigned subsystems.

Weekly in-person meetings with all members as well as several subteam meetings per week throughout the academic year resulted in effective communication and a broader understanding of all systems amongst team members. Numerous testing periods have been completed since the fall semester to test turbine components regularly throughout the design process. These events also encourage participation and are invaluable to new members' understanding of the assembly as a whole. Testing results have proven that the team's research, calculations, and careful consideration in designing each component has been worth the effort.

Blades

Airfoil Selection

This year, the team's goals were to improve upon previous years' methods for blade design and manufacturing and work to validate theoretical results. The team researched various airfoils such as the SG6043, Wortmann FX 63-137 13.7% smoothed, ISA 961, MH 114 and Eppler 396 due to their optimized shapes for high lift. These airfoils were considered for their higher thickness-to-chord ratios or their high lift-to-drag ($\frac{C_l}{C_d}$) ratios to increase efficiency and power production. A greater thickness-to-chord ratio improves the structural rigidity at the root of the blade, while an airfoil with a higher lift-to-drag ratio optimizes aerodynamics at the blade tip. One approach taken by the team to increase power production was to use the methods outlined in a research study specifically focused on small-scale wind turbine applications. The design method was replicated using XFLR5 with reference airfoil SG6043. Based on the initial research, the team optimized the thickness/camber ratio as compared to its base airfoil, ultimately creating the EYO 7-8 seen in Figure 2 [1]. Results showed that the optimal

thickness-to-camber ratio for improved blade performance lies in the range of 0.85-1.50 [1]. This ratio translates to a higher $\frac{C_l}{C_d}$, to increase turbine efficiency and power production.

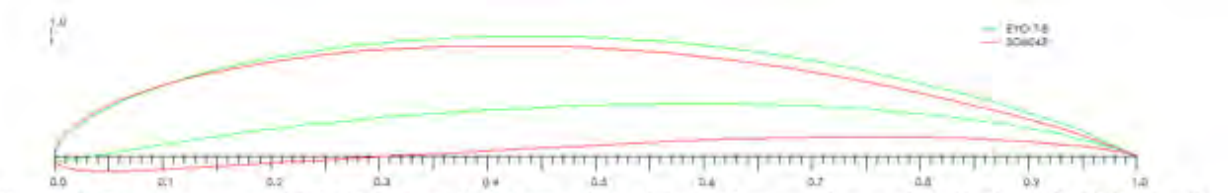

Figure 2. Newly created EYO 7-8 airfoil (green) and its reference base airfoil, the SG6043 (red).

An example of the validation for this increased $\frac{C_l}{C_d}$ ratio, computed using XFLR5, was plotted versus angle of attack ($\propto$) at a Reynolds number of 50,000 (Figure 3). The lift-to-drag ratio was greater for the optimized airfoil shape, EYO 7-8 for various Reynolds numbers ranging from 20,000 to 100,000.

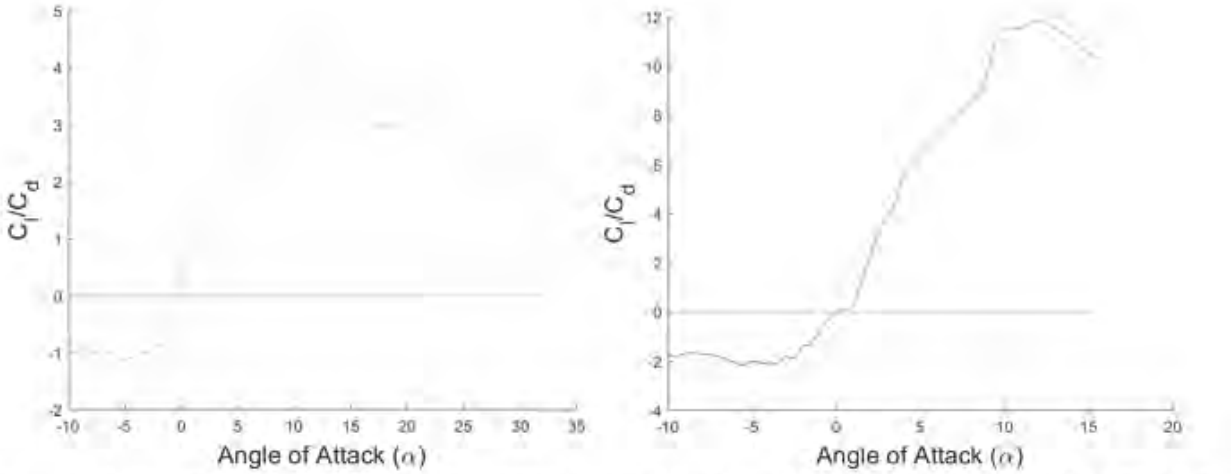

Figure 3. Lift-to-drag versus alpha for the EYO 7-8 airfoil (right) and SG6043 airfoil (left). The EYO 7-8 had a max lift-to-drag ratio of 11.9 while the SG6043 had a max lift-to-drag ratio of 4.2.

Blade Design

The blade design optimization process utilized the team's in-house Blade Element Momentum Theory (BEMT) MATLAB code. The program takes into account CWC scoring to optimize the chord and twist distribution for lower wind speeds as well as modifies variables such as tip-speed ratio (TSR), chosen airfoils, and the transition point between the root and tip airfoils. Based on the theoretical Power Curve points and cut-in wind speed generated by the program, the team down-selected from more than 20 possible root and tip airfoil combinations. Although cut-in wind speed is not a competition factor this year, the team recognized that a lower cut-in speed is preferred to ensure that power is generated when scoring begins at 5 m/s. The team validated the results of the BEMT code by using a Betz optimization method; the Betz optimization produced blades with a very similar chord and twist distribution to the BEMT code.

The BEMT code has a feature to produce chord and twist values at each of the fourteen chosen segments along the blade as well as the airfoil at each segment. A cylindrical base, designed to fit into the mechanical pitch control system, was added to the blade. Then, the comprehensive design was uploaded into QBlade for interpolation of the remaining airfoils between the root and tip.

Chord and Twist Design

From the BEMT optimization code, two blades were ultimately chosen based on theoretical performance values. Blade Design 1 used the SG6043 as the root airfoil transitioning at 50% of the radial position to a newly designed EYO 7-8 airfoil at the tip and was optimized for a TSR of 2. Blade Design 2 was entirely composed of the Wortmann FX 63-137 13.7% smoothed airfoil and also optimized for a TSR of 2. Both blades are presented in Figure 4.

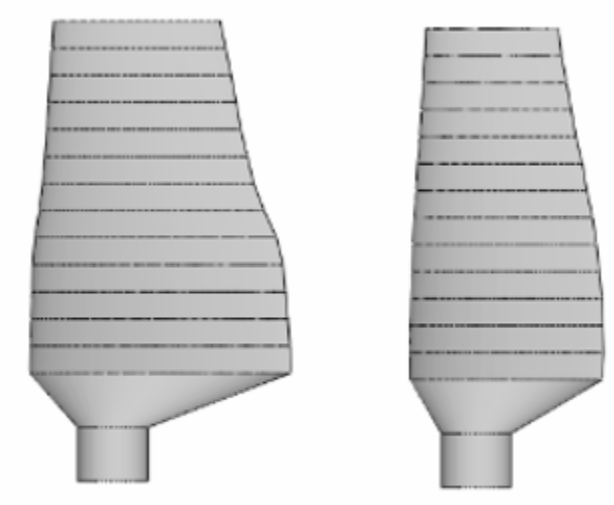

Figure 4. Blade Design 1 (left) and Blade Design 2 (right) finalized using Qblade.

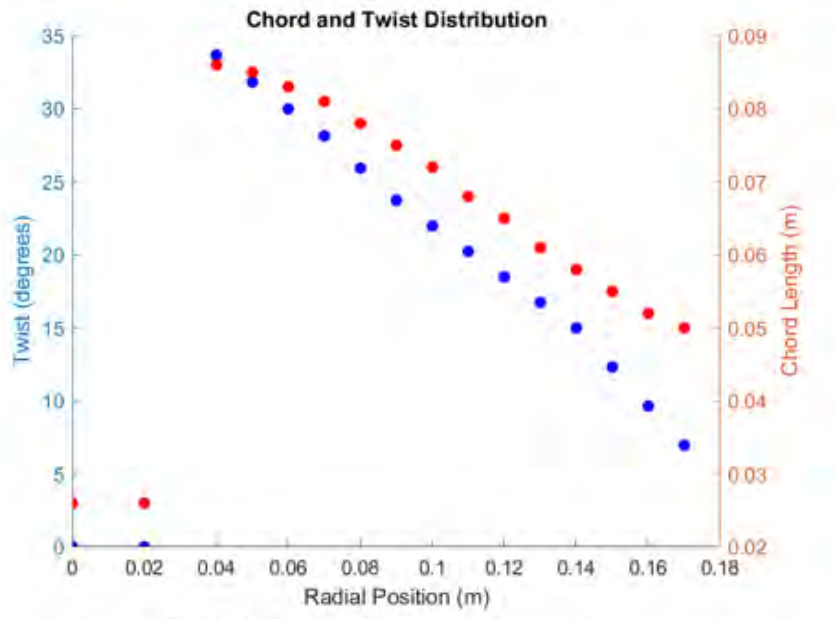

Figure 5. Blade Design 2 chord and twist distribution.

It should be noted that Blade Design 1 featured a significantly wider root chord than Blade Design 2. The team believed the wider root of Blade Design 1 would allow the blade to have a lower cut-in speed and better performance at lower wind speeds. However, Blade Design 2, which had similar power performance based on theoretical results, has a shape more comparable to industry standard blades. Ultimately, based on experimental data (discussed further below), Blade Design 2 was selected as the final design. The chord and twist distribution of this blade are shown in Figure 5.

Blade Manufacturing

Initial versions of the blades were created using either 3D printing of PLA or a hand layup method. The initial 3D printed blades were manufactured at 100% fill. 3D printing methods were chosen for rapid prototyping due to ease, precision, and replicability. Hand layup blades were made using a laser-cut balsa skeleton wrapped with fiberglass and covered with epoxy. The layup method was attempted to further reduce the blade weights and replicate methods similar to that in industry.

The team selected the 3D printed method to create the final blades to limit manufacturing errors and variability; the layup method created unequal weights and surface finishes across each blade due to a lack of process control when applying epoxy. The 3D printed method also left an imperfect surface due to the printing resolution, so the blades were sanded down using 220 and then 600 grit for a final, smooth product shown in Figure 6. To mimic the goal of the hand-made blades, the final sets of blades were manufactured using 20% fill to reduce the weight of the blades while maintaining structural rigidity. In response to a failure that occurred during testing, an infill of 60% was used in the cylindrical base to provide additional rigidity to the spar holes. The failure was caused during a runaway condition where the spar hole in the center blade fractured, as shown in Figure 7. This resulted in the shear failure of the other two blades, releasing all three blades from the hub. Figure 7 also shows how each blade broke towards the root, and then upon impact with the testing safety glass.

Figure 6. Finished Blade

Figure 7. Blade Failures at the Root

Blade Performance

Theoretical and experimental data taken from the power curves can be non-dimensionalized and compared by plotting the coefficient of power (C_p) versus the tip-speed ratio (λ). The theoretical and experimental plots are presented in Figure 8.

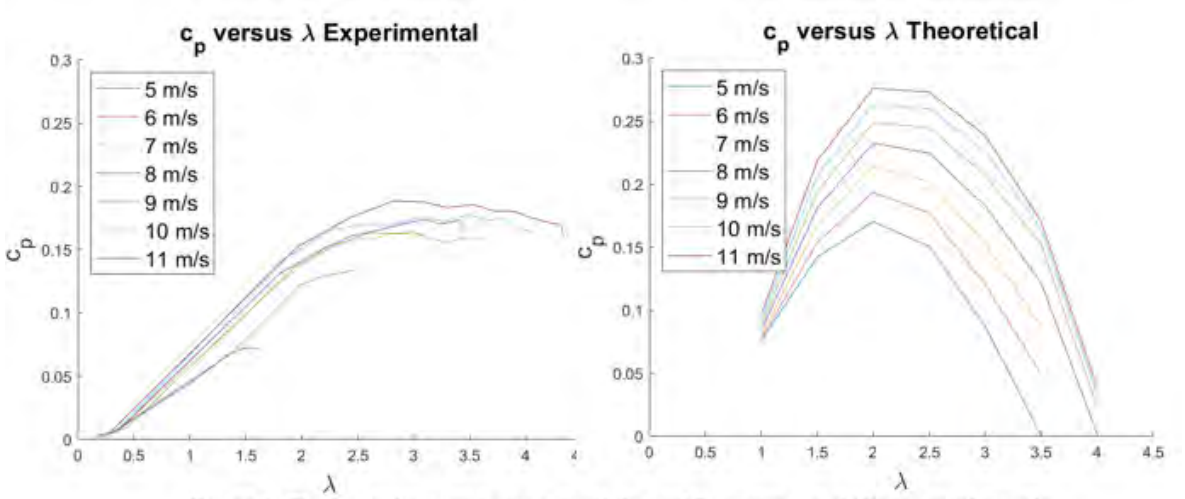

Figure 8. Theoretical versus experimental data of C_p versus λ at different wind speeds.

The maximum power from the experimental data at each wind speed from 5 to 11 m/s was used to estimate the Annual Energy Production (AEP). All wind speeds below 5 m/s were assumed to generate 0 W, and rated power was set equal to the maximum power generation at 11 m/s. The AEP was calculated using Equation 1, where V is the wind speed:

$$AEP = (Operating\ Hours\ Per\ Year) \int_0^\infty (P(V))(Probability(V))\, dV \quad (1)$$

The probability term refers to the cumulative probability that a wind speed is between 0 m/s and 22 m/s, calculated using a Weibull distribution. This integral was calculated numerically by utilizing the cumulative probability of the wind speed in 1 m/s bins.

$$f(V_1 < V < V_2) = exp(-(V_1/A)^k) - exp(-(V_2/A)^k) \quad (2)$$

A value of 7.34 m/s was chosen for A, representing the average wind speed in the Galveston-Gulf Coast area - the location of VTexas' utility scale wind farm for this year's siting competition. A value of 2.28 was assumed for k [2]. This integration suggests that the blades will produce 55.8 kWh/year under a capacity factor of 100%. If the blades were to operate at a capacity factor of 50%, closer to that of the offshore wind power industry, they would produce 27.9 kWh/year. When calculating the AEP using the theoretical max power values instead, the blades are predicted to produce 81.5 kWh/year and 40.7 kWh/year, respectively. These values are notably higher than the experimental values. The team believes this difference comes from inefficiencies in the mechanical and electrical systems as well as the inability to adequately model the aerodynamics of a small scale wind turbine with BEMT.

Mechanical Systems

Introduction

The primary goal for this year's competition was to redesign inefficient mechanical subsystems. With a considerable number of returning members from previous years, the team looked to capitalize on technical knowledge and experience to innovate and design systems to facilitate multiple competition tasks. For improved performance during the Power Curve, Safety, and Durability tasks, the team focused on redesigning the pitch control and hub systems. With the addition of the offshore simulation task, the team also spent a considerable amount of time researching, designing, and testing a fixed-bottom offshore foundation.

The only subsystems that remained unchanged were the yaw system and tower, as they proved to

be sufficient in previous years. Additionally, the mechanical brake of last year's design was removed to decrease the size of the assembly and simplify power systems and controls during operation.

Pitch Control and Hub

The previous pitch control system was able to pitch a total of 30°, encompassing cut-in and power angles. However, the lack of range proved insufficient for controlling rotational speed at high wind speeds, and the system would also struggle to maintain blade alignment. This resulted in the decision to redesign the pitch control and hub system to increase range and efficiency, reduce size, and minimize components. Table 1 shows how pitch control will be used for each task with anticipated angle of attack.

Table 1. Pitch Control

Competition Task	**Approx. Angle**	**Pitch Control Purpose**
Power Curve Performance	0° (vertical)	Pitching the blades to the angle that produce the most power at $5 - 11\frac{m}{s}$ wind speeds
Safety	-10° or 90°	Pitching the blades to stall or feather to stop the turbine
Durability	45°	Pitching the blades to feather to reduce the loads applied on the turbine and help the foundation's stability

The design process began with an extensive concept generation phase. At first, the team brainstormed alternatives to the actuation portion of the old pitch control system. Some early concepts included a linkage system, rack and pinion, and hydraulic actuation. Through additional research, the team found a potential hub alternative based on the swashplate pitching system used in RC helicopters. As a result, the team decided to broaden the scope of the engineering problem and reconsider the hub design as well. The team ultimately used a two-part weighted decision matrix to down-select concepts, as seen in Table A1 (Appendix). The matrix was split into two categories: (1) rotational-to-translational concepts on the baseplate and (2) translational-to-blade rotation in the hub.

The conceptual design phase helped define the design requirements for both subsystems. For baseplate actuation, key criteria included simplicity, back-drivability, precision, and range. The hub actuation comparison considered similar criteria while also considering precision of blade alignment. The winning concept from the decision matrix was the stepper motor and linkage system with RC pitching in the hub. A stepper motor and linkage connection allowed for quicker actuation in comparison to lead screw or rack/pinion designs, while also reducing the size of the system. Influenced by the swashplate mechanism in RC helicopters, the RC pitching concept was beneficial in preventing blade misalignment.

The team struggled to quantify the exact friction provided in the linkages and connections to balance stepper motor function and prevent back-driving; the team did not feel confident in a linkage connected directly to the stepper motor, as it seemed too susceptible to back-driving. Consequently, to add mechanical advantage to the system, the final pitch control design included a set of gears connected to the stepper motor.

The final pitch control system with labeled components is shown in Figure 9. The pitching system converts translational motion within the drivetrain to rotational motion of the blades. The system operates by a dual shaft stepper motor **(a)** connected to two small gears on each side **(b)** in mesh with larger gears below **(c)**. The larger gears rotate together via a shaft fixed with a set screw and also act as an alignment tool for the linkages **(d)**. The first linkages connect to a moving bearing block **(e)**, which actuates along a set of linear rails **(f)**. As the large gear rotates, it pushes the linkage forward, actuating the bearing block either forward or backward. The bearing block houses a bushing **(g)**, which is fixed relative to the bearing

block using an external snap ring. The purpose of the bushing is to act as a connection point to the swashplate **(h)** and provide added rigidity to the connection between the hub and pitching system. The second set of linkages **(i)** are connected to the swashplate and to the base of the blade holster **(j)**. As the swashplate actuates, the linkages also move forward simultaneously, allowing for nearly 90° of pitching while maintaining blade alignment.

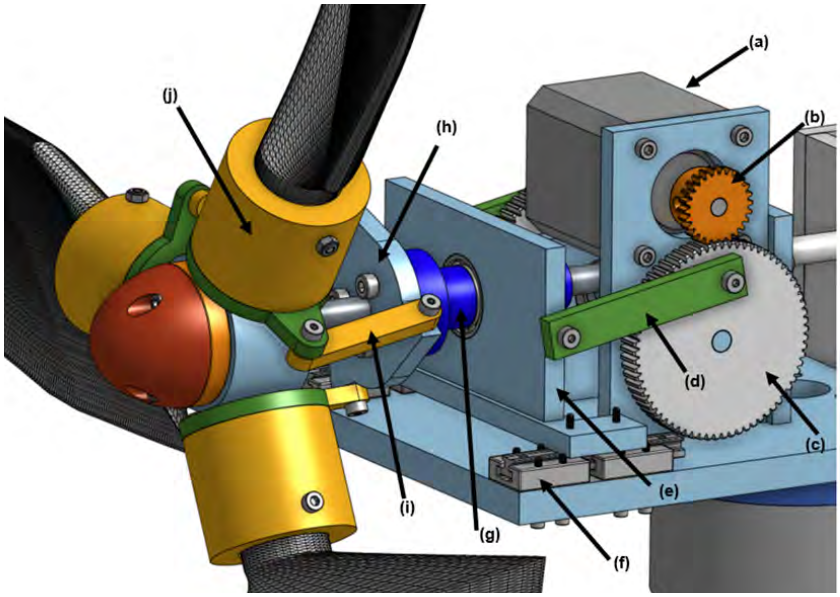

Figure 9. Pitch control assembly with labeled parts

To validate the pitch control system design before manufacturing, the team checked for (1) the minimum length of actuation required for 90° of pitching and (2) back-drivability at different linkage angles. To define the length of linkage attached to the hub, the team determined how much distance the blade holster tab had to travel to allow 90° of rotation in the blade holster. As seen in Figure 10, the distance, D, was defined by Equation 3.

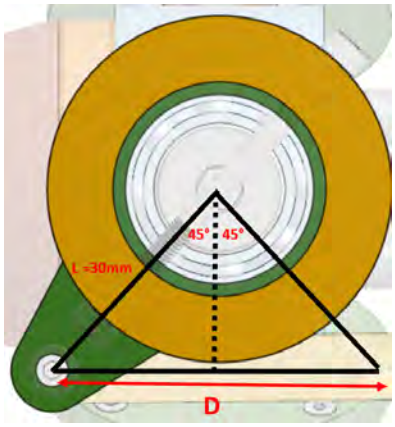

Figure 10. Blade holster linkage relationship

$$D = L * 2sin(45) = 30mm * 2sin(45) = 42.43\,mm \quad (3)$$

With the distance of travel defined, the team was able to move forward in designing the length of the linkages in the system. To ensure the system would not back-drive during operation, the team ran a Matlab analysis to determine the equivalent force required to actuate the swashplate based on the moment created by the blades at $22\frac{m}{s}$ operating conditions. The moment created by the wind was integrated over the length of the blade, defined below:

$$M_{blade} = 0.15c^2 * 0.5 * \rho_{air} * V^2 = \int_0^r \frac{0.2}{2} * c(r)^2 * \rho_{air} * [U_\infty + (\omega r)^2]\, d(r) = 0.1221\, N \cdot m$$

where c is the chord length, r is the distance from the blade root, U_∞ is the maximum incoming wind speed ($22\frac{m}{s}$), ω is the angular blade velocity ($196.4\ \frac{rad}{s}$, based on TSR =2), and ρ_{air} is air density ($1.225\ \frac{kg}{m^3}$). Using this calculation, the team was able to determine the amount of force the linear swashplate would have to apply to the system to avoid back-driving. As shown in Figure 11 and Equation 4, the equivalent force was calculated based on the moment and its distance from the force. The plot in Figure 11 shows the varying magnitude of force based on the angle of the linkage, θ.

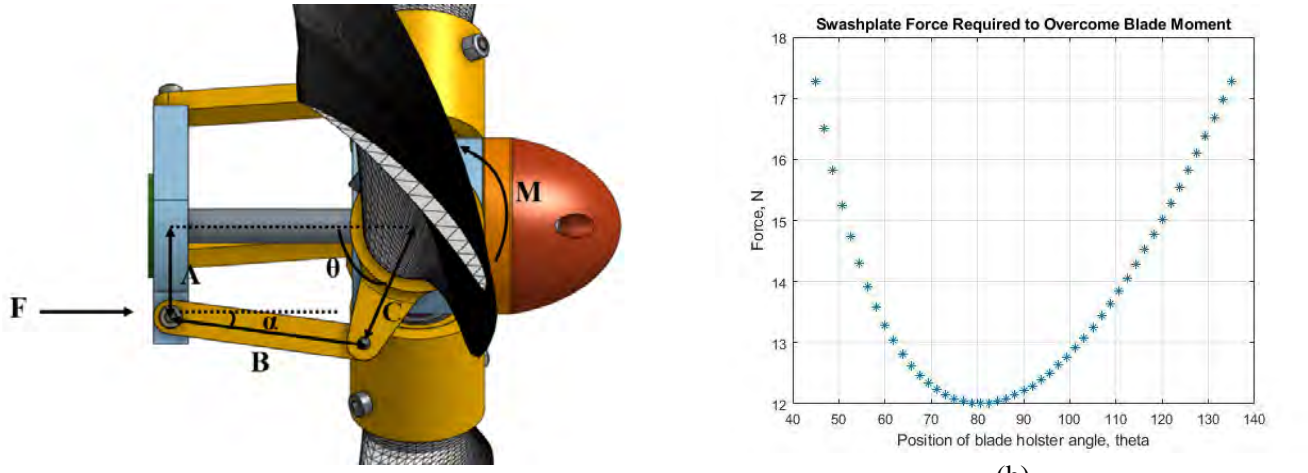

(a) (b)

Figure 11. (a) Geometrical relationship between moment and force (b) Swashplate overcoming force as a function of linkage position

$$F_{swashplate} = \frac{3Mcos(\alpha)}{Csin(\alpha+\theta)} \quad (4)$$

Using the maximum equivalent force on the swashplate, the team calculated a back-driving factor of safety (FOS). To actuate the distance, D,that would achieve 90° of pitching, the rear linkage would have to be at least 3.0 cm long, resulting in a torque on the stepper motor that exceeds the holding torque of $44\ N \cdot cm$. This calculation justified that the gear ratio added to the system was necessary to prevent system back-driving.

$$T_{stepper\ motor,\ no\ gearing} = F_{swashplate,\ max} \times L_{linkage} = 17.27N \times 3.0\,cm = 51.81\ N \cdot cm$$

$$FOS_{no\ gearing} = \frac{T_{stepper\ motor,\ holding}}{T_{stepper\ motor,\ no\ gearing}} = \frac{44\ N{\cdot}cm}{51.81\ N{\cdot}cm} = 0.85,\ not\ desirable$$

The team wanted a FOS of at least 2.0 regarding system back-driving which required a gear ratio of at least 1.49. Gearing was selected based on stock gear availability. The two selected gears had 26 and 70 teeth, respectively, yielding a gear ratio of 2.69. This result gave the team reassurance that the blades will not back-drive during normal operation when the stepper motor is being powered.

$$T_{thrust} = T_{big\ gear} = F_{swashplate,\ max} \cdot R_{big\ gear} = 17.27\ N \times 1.9\ cm = 32.81\ N \cdot cm$$

$$FOS = \frac{T_{stepper\ motor,\ holding}}{T_{stepper\ motor,\ allowable}} = 2.0$$

$$T_{stepper\ motor,\ allowable} = T_{small\ gear} = \frac{T_{stepper\ motor,\ holding}}{FOS} = \frac{44\ N{\cdot}cm}{2.0} = 22\ N \cdot cm$$

$$Gear\ Ratio = \frac{N_{big\ gear}}{N_{small\ gear}} = \frac{T_{big\ gear}}{T_{small\ gear}} = \frac{32.81\ N{\cdot}cm}{22\ N{\cdot}cm} = 1.49$$

In previous years, the hub design has been a cause of cracking failures due to high stress concentrations in its geometry. The goal of the new hub design was to simplify the assembly process, while increasing the system durability to operate at higher wind speeds. As seen in Figure 12, each blade **(a)** is fastened to the blade holster **(b)** with a set screw. A radial thrust bearing **(c)** was selected to withstand the high centripetal forces experienced during operation; the bearing is press-fit into the blade holster but also fastens from the bottom with the spar holder ring **(d)**. The geometry of the blade holster and spar holder ring was designed specifically to apply compression to the outer raceway of the bearing, allowing the bearing balls to rotate freely with respect to the inner raceway. A shoulder screw **(e)** fastens the blade assembly to the hub core **(f)**. A steel shaft collar **(g)** clamps down on the keyed drive shaft **(h)**, and the collar also includes holes for the nose cone **(i)** attachment. The nose cone's function is to reduce aerodynamic drag.

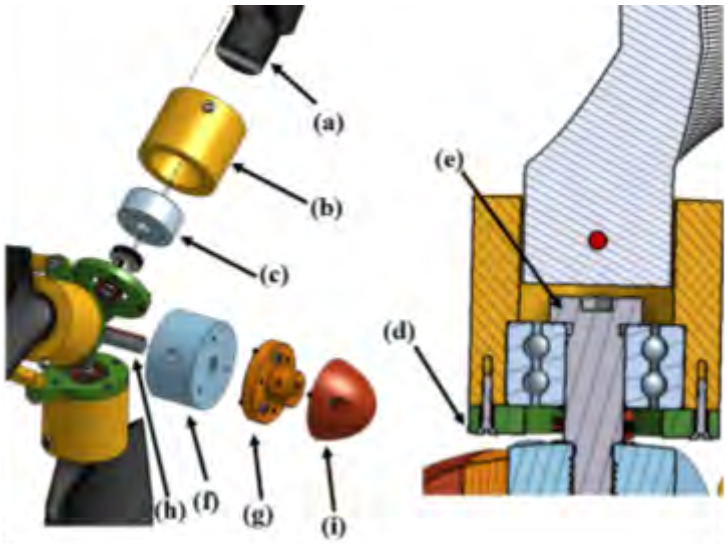

Figure 12. Labeled Hub Assembly

Foundation

To address this year's offshore foundation challenge, the team conducted research and experimentation with a wide variety of foundations inspired by industry standard designs. Simple, low-weight designs were prioritized for manufacturability and ease of installation. Several iterations of a box and cylinder type design were made and tested, ultimately giving the team a successful foundation design that performs well at all competition wind speeds. Table 2 summarizes the experimentation and designs explored during the foundation design process.

Table 2. Foundation Designs and Modes of Failure

Iter. #	Type	Installation Method	Reason	Foundation	Failure Point: Reason
1	Concrete Vibrator	Concrete vibrator to fluidize the sand to allow the plate to slide through the sand	Easy installation of subterranean plate	Subterranean plate	Installation: Sand was too viscous
2	Water Jet	Water jet to blast away sand below the plate as it is being installed	Easy installation of subterranean plate	Subterranean Plate	Installation: Insufficient sand affected
3	Suction Caisson	Pump to remove water from the interior of the bucket and pull the system down into the sand	Create suction within caisson to increase sand effective strength	Caisson	14 m/s: Overestimated compressive force of sand and lack of maintained suction
4	Internal Spiral	Crank to screw the system into the sand.	Prevent piping to allow suction to be maintained	Caisson	Installation: Excessive friction between internal fins and sand caused sand to rotate rather than allowing the system to be installed.
5	Manual Excavation	Box to prevent backflow of sand and posthole digger to remove sand from the box interior.	Easy installation of subterranean plate	Subterranean plate	19 m/s: Deflection of the plate reduced strength of the design and ability to utilize the weight of the sand effectively.
6	Finned Box	Pump water out from the interior to suction the system into the sand.	Maximize contact area with the sand and in turn maximize compressive and friction forces	Finned box	None: None

Last fall, the team attempted alternative methods for installation of the plate design under the sand including a concrete vibrator and water jet, each intended to fluidize the sand allowing the foundation to be slid through the fluidized sand. These methods proved insufficient for achieving the necessary viscosity of the volume of sand that needed to be fluidized. Additionally, a manual excavation method using a box and posthole digger was developed and tested, but deflection of the plate led to insufficient foundation stability.

The first foundation tested was a suction caisson seen in Figure 13. Various calculations were used to analyze the forces in the caisson design before testing. To determine the forces on the turbine,

Figure 13. Suction Caisson Foundation Design

drag forces on the yaw tails were calculated, and Betz's law was used to determine forces on the blades. To calculate the forces in the foundation, a center of rotation was determined based on an equalizing of horizontal forces. Next, experimental data was gathered to estimate a friction coefficient of sand on steel, and effective stresses of the sand were calculated. Finally, the weight of the turbine was compared to the effective stress of the sand to determine the mode of failure, and this was factored into the total overturning moment. Based on the calculations, the compressive forces provided most of the system's stability in the sand with a total factor of safety of 1.95 for the design.

In testing, this design was installed by inserting a metal cylinder into the top layer of sand, then pumping water out through a vacuum port to create a differential pressure that pulled the structure further into the sand. After failure during wind tunnel testing, the team recognized that the high permeability of the sand made suction nearly impossible. Further investigation revealed that the cohesion factor of sand is generally considered to be zero; and industry practice does not suggest installation of suction caissons in coarse-grained soils. Additionally, the effective and friction stresses of the sand were insufficient to oppose the maximum overturning moment of the wind.

However, the effective and friction stresses supported the caisson with minimal deflection at wind speeds up to 14 m/s. The structure remained in place and mostly upright when the wind speed was brought up to 22 m/s but deflected more than 6 mm. As a result, the team designed two alternative concepts (finned box and internal spiral) that increased the contact area of the foundation with the sand to maximize these forces and to attempt to establish a permanent suction within the caisson. The team attempted to test these new designs for comparison with the first iteration.

The majority of the deflection while using the box design appeared to result from elastic deflection of the top plate – shown by the tower returning to its original position once the wind speeds were reduced to zero. A second iteration of this design increased the thickness of the top plate, and diagonal fins were welded in as cross braces for additional reinforcement. This is anticipated to result in less deflection than that of the original suction caisson design.

The internal spiral design, which utilized the structure of the previous suction caisson, implemented a gradient spiral fin running along the inside of the cylinder to prevent piping of the sand and potentially allow suction. This design was to be installed by rotating the system into the sand like a screw. This design also failed, as the sand inside the system started to rotate with the caisson due to high friction, making installation impossible.

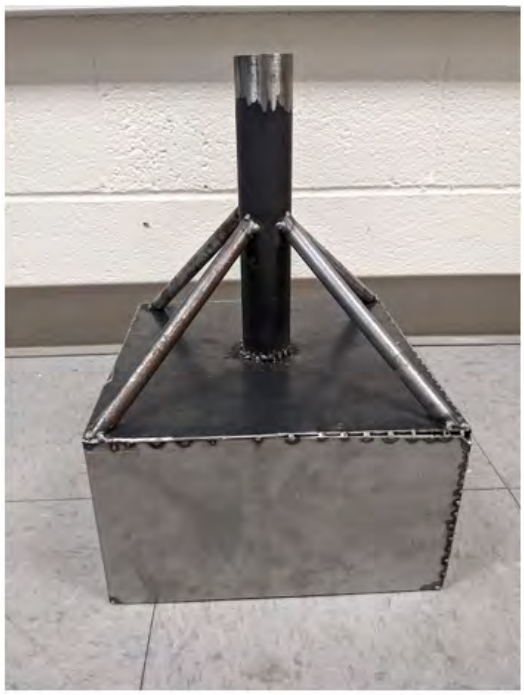

Figure 14. Final Finned Box Foundation Design

The finned box design, seen in Figure 14 was selected as the final foundation design for multiple reasons. The square design allows for maximum utilization of the sand's effective and frictional strength. A skirt thickness of 1/32 in. was selected to reduce weight, while the lid was increased to 5/64 in. to eliminate elastic deflection. The cross braces, as discussed previously, also have a thickness of 1/32 in. to reduce weight. The braces were placed in an x shape rather than a + shape to provide the maximum projected area perpendicular to the wind load, should the tank be rotated after foundation installation. To allow water to escape the system during installation, a single hole was drilled into the lid, and small slots were cut into the tops of the cross braces. Finally, braces were added between the four corners and the tower to make the system even more rigid and prevent deflection of the lid.

Because the caisson failed far below the expected parameters, modifications to the calculations were made for the finned box analysis. The error seems to derive from the effective strength of the sand being lower than expected. Using the failure point of 14 m/s of the suction caisson and separating out the effects from friction, a new compressive strength of the sand was determined. Based on these calculations it was determined that the original compressive strength of the sand was off by a factor of 5.41. Updating the calculations with the new effective strength of the sand, the factor of safety of the finned box design came out to be 1.242 as calculated in the equations below with the majority of the resisting forces still coming from the compression of the sand. To increase this value, it is proposed that mass be added to the tower to increase the overturning moment provided by the weight of the system without raising the center of mass or increasing the mass of the foundation.

$$M_{effective\ stress} = 81.837\ N * m$$
$$M_{friction} = 4.003\ N * m$$
$$M_{Lid} = 4.316\ N * m$$
$$M_{Total} = M_{effective\ stress} + M_{friction} + M_{Lid} = 81837 + 4.003 + 4.316 = 90.156\ N * m$$
$$M_{Required} = (F_{Blades} + F_{Yaw}) * (h_{turbine} + h_c) = (54.76192 + 13.02) * (1 + .0713) = 72.615\ N * m$$
$$FoS = \frac{M_{Total}}{M_{Required}} = \frac{90.156}{72.615} = 1.242$$

Power Systems and Controls

Introduction

The main goal of the team this year was to improve upon subsystem designs from previous years and come up with creative yet simple solutions to the competition tasks. With a team of mostly new members, the first discussions involved familiarization with both working and non-working designs of the previous year, and how certain competition provisions, such as 120 VAC power on the load side, could be taken advantage of to innovate further. The team's primary focus centered around power optimization and regulation, specifically from the load side and developing a reliable communication scheme between the turbine-side and load-side subsystems. This year's chief innovation is the utilization of an electronic variable resistance load or universally controllable load (UCL) that serves both as a replacement of a static load resistor and a control mechanism. With this additional layer of versatility, the team has achieved power optimization, generator voltage regulation, and dynamic response capabilities which have greatly improved our performance overall. The control systems design is highlighted by the use of an STM32 microcontroller and a finite state machine method of control organization, making it simple to determine which system runs during a specific competition task, and limiting the number of moving parts that need to interact, as all the controls run through the same microcontroller. The one-line diagram for the full electrical system is shown in Figure 15.

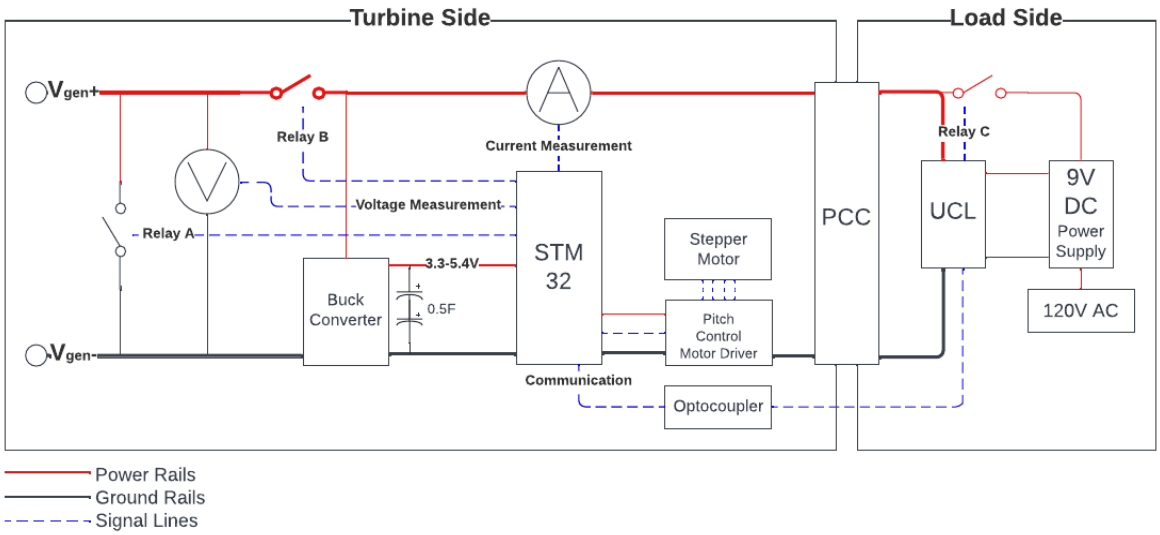

Figure 15. Complete one-line diagram of electrical system

Generator Selection and Analysis

This year's generator was selected based on knowledge of last year's power production and the expectation of generating equal or more power this year. A Maxon RE-50 brushed DC generator was selected on the basis of its size, voltage and current constants, and torque specifications. Knowing the previous years' best possible blade performance and power generation, the voltage and current constants were selected to achieve a cut-in below 5 m/s wind speed, without compromising how much voltage would be produced. Rather than dedicate time to building a custom generator, the team opted for an off-the-shelf component to invest time and resources into aspects of the control system. Choosing the RE-50 early also allowed the team to design around it, as opposed to selecting a generator based on the blade performance, which would be more difficult due to constraints of what generators are commercially available. Additionally, having the generator ahead of time helped streamline the design of a generator braking system, as it could be tested immediately and tweaked as necessary.

Universally Controllable Load Design

The universally controllable load (UCL) was designed as a means to eliminate the need for a single load resistance value – optimized for power at only one wind speed – and to replace this single value with a controllable load resistance. The implementation uses a voltage-controlled current sink (MOSFET) in a closed-loop configuration (Figure 16) which allows fine adjustment of the current independent of the applied voltage. The design enables a far higher degree of controllability when compared to a more traditional single-resistance load. In particular, by incorporating an Arduino Nano microcontroller into the design, the UCL can operate in several different control modes including constant-current, constant-resistance, constant-power, constant-voltage, and maximum power point tracking (MPPT), the latter of which is used during the Power Curve task.

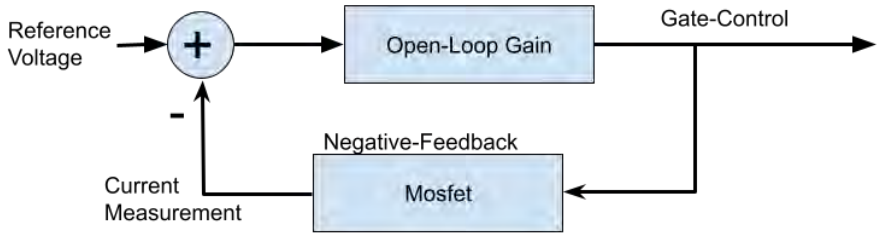

Figure 16. UCL feedback mechanism

The MPPT control mode is particularly important, as it allows for maximum power extraction at any wind speed. This is accomplished by matching the impedance of the load (UCL) with the equivalent impedance of the generator, a dynamic parameter which depends on wind speed among other factors. A well-known algorithm called *perturb and observe* is implemented here, shown in Figure 17. The primary advantage of choosing this algorithm is its minimal input requirements; i.e. it relies solely upon power measurement and does not require additional sensory inputs from the turbine-side systems. The MPPT system also reduces the need to fine tune the pitch control at each wind speed to maximize power. Instead this optimization is achieved at a single pitch angle, thereby reducing system complexity and power usage.

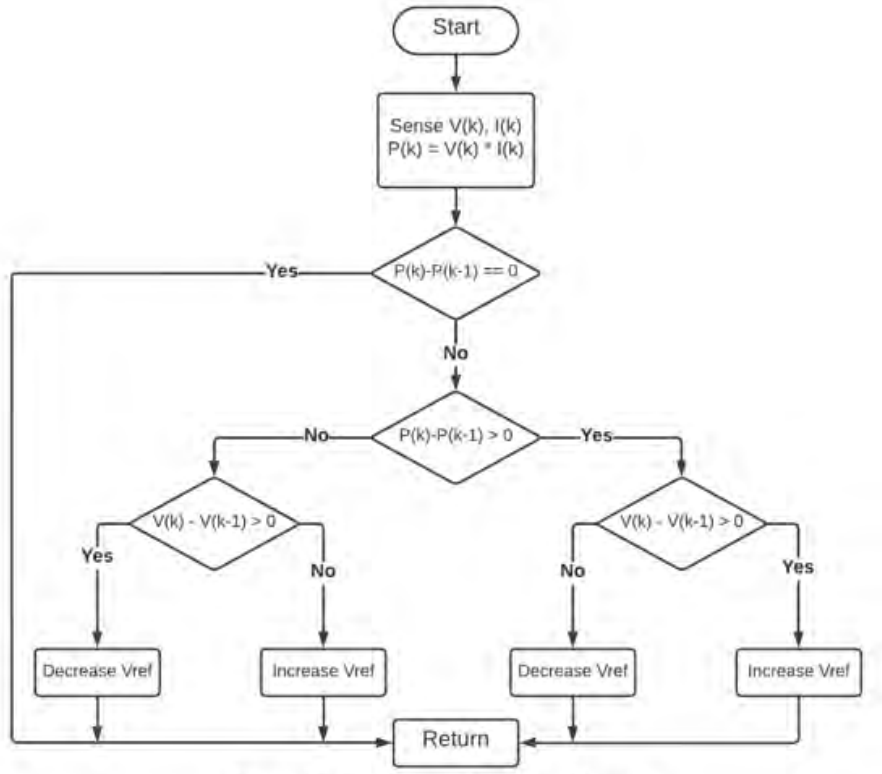

Figure 17. Perturb and Observe Algorithm

In addition to power optimization, the UCL provides a power and voltage limiting mechanism for the Durability task, an optimal cut-in condition, and an auxiliary power source for use during the shutdown phase of Safety Task. The constant-power control mode is used to maintain the turbine power output regardless of wind speed which satisfies the positive power requirement of the Durability Task. Voltage limiting is achieved on top of this which protects turbine-side systems and has the added benefit of preventing a run-away condition of the turbine. Values of 30W and 15V have been chosen for the

power and voltage limits respectively. Finally, to take advantage of the auxiliary power available on the load side of the point of common coupling (PCC), the UCL has a relay which can direct 9V power onto the PCC lines to power turbine-side systems during the shutdown phase of Safety task. When auxiliary power is enabled, the load itself is in an open-circuit configuration.

Crucial to the operation of the UCL is its communication with the STM microcontroller on the turbine side. This is achieved with the use of an optocoupler which isolates turbine side and load side systems, thereby preventing unwanted power-flow. The UCL functions in tandem with the finite state machine logic, described in detail below.

Finite State Machine Design

The Finite State Machine (FSM) control system for the turbine was designed to fit the requirements of the CWC. The FSM is composed of four states: Safety, Cut-In, Durability, and Power, as shown in blue in Figure 18. The safety state, initiated by one of two triggers, represents an active state of either manual safety button press or a detected disconnected load. In the event of a safety trigger, several steps take place to brake the turbine and prepare the on-board electronics for shut-down. First, the pitch control adjusts the blades to their optimal braking angle, then Relay B is opened to isolate the generator and Relay A is closed to apply EMF braking. Finally, the UCL is sent a command to apply auxiliary power over the PCC. The cut-in state represents the turbine's initial start up from a stationary state. In this state, blades pitch to an optimized position for low wind speeds, and the UCL emulates an open circuit to allow the system to cut-in at the lowest possible wind speed.

The durability state represents the turbine's operation in high wind speeds. In this state, turbine components work to prevent runaway and minimize the load on the turbine, through both the UCL and the pitch control system, resulting in a low, constant power output. The final state, power, represents the turbine's operation in the power performance range of 5m/s - 11m/s wind speeds. During this time, the blades pitch to the point of maximum power transfer, and the UCL actively tracks the maximum power point and adjusts the load resistance accordingly.

All of these states are held in the memory of the STM32 microcontroller, and powered either by the turbine, or for a finite period of time by two supercapacitors, capable of powering the STM32 while it completes reset procedures before losing power.

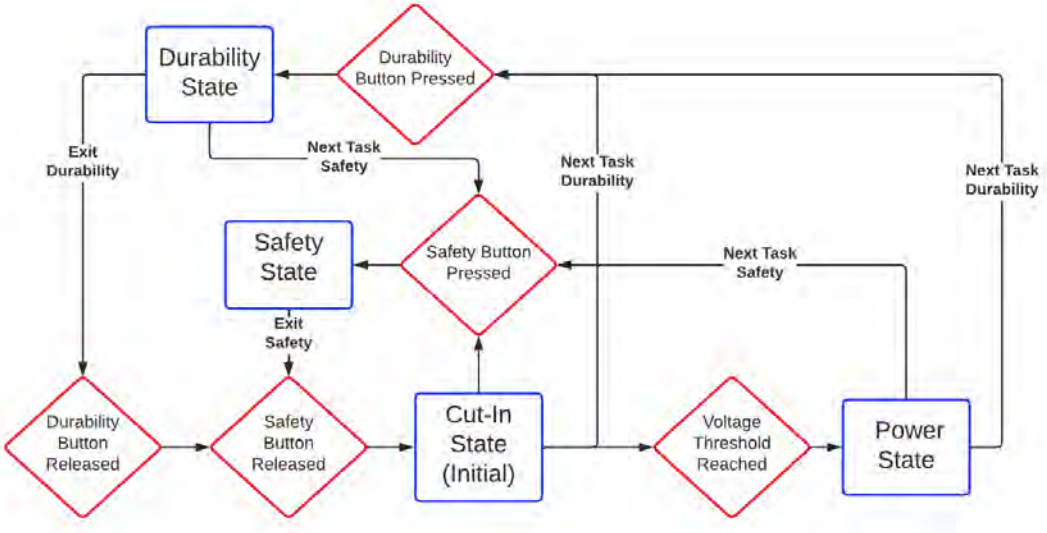

Figure 18. Finite State Machine Logic Flowchart

Control of Inputs and Outputs

In order to interface the electronic controls with both electrical and mechanical subsystems, the STM32 microcontroller requires a large set of inputs and outputs to receive and transmit data. The electrical components being interfaced with include: the buck converter, hall effect current sensor, voltage sensor, stepper motor driver, relays, and UCL, which includes the extra constraint of optical isolation due to its position on the load side of the PCC. The inputs received by the STM32 include a regulated voltage from the buck converter, responsible for powering the STM32 at 3.3V, as well as voltage and current values originating from test points in the system which are scaled down to be measured through GPIO pins and scaled up appropriately to determine their values. The outputs from the STM32 include the power and instructions necessary for the motor driver to operate the stepper motor during blade pitching, and voltage pulses to switch relays in accordance with the present task. The STM32 also interfaces with the UCL, both transmitting data about its current state and receiving data about the voltage, current, and power at the PCC. This data line is isolated with an optocoupler, so that no power is transmitted across the PCC without going through the main power wires. Both the GPIO pins and two analog to digital converters (ADCs), were configured using STMicroelectronics STMCubeIDE tool. The chip configuration is shown in Figure 18. Pins PC11 and 10 are configured as UART input/outputs, for communication with the load side circuit. Pins PA0 and PA4, which measure current and voltage are connected to the shared ADC. A user defined function was implemented to switch between the two ADC channels. The hall effect current sensor reading was calibrated according to its datasheet voltage-current relationship curve, reading a measured voltage and converting it to the perceived current. Pins PA10-12 control the relays by sending digital rising or fall edge signals. Pin PB2 polls the safety state button to signal entrance into the safety state of the FSM. Pin PA9 polls the durability state button, similarly used to signal entrance into the durability state of the FSM, as controlled by a manually pressed button. Pins PC7-9 control the stepper motor responsible for blade pitching. These pins provide the microcontroller with the interfaces necessary to control the turbine and adjust its operating state.

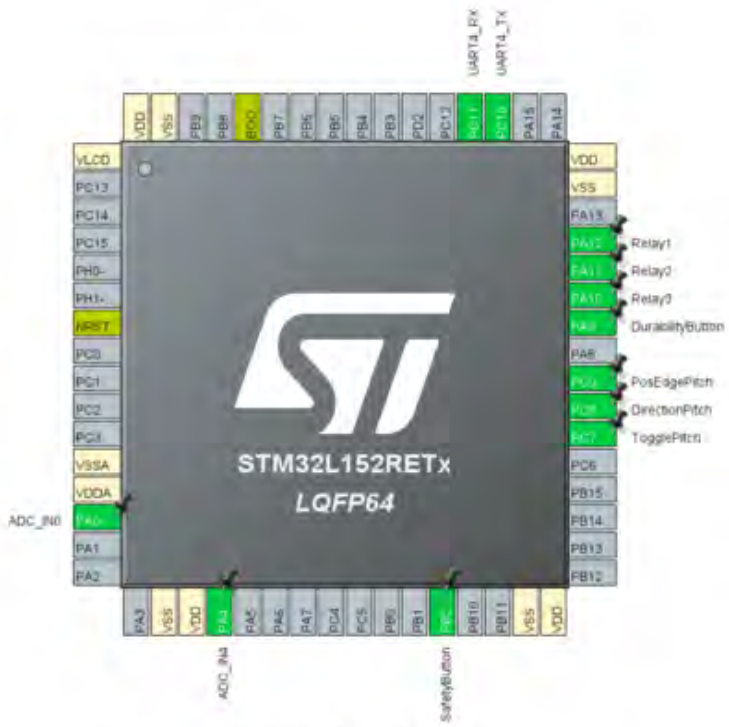

Figure 19. STMCubeIDE chip view

Aside from the electrical subsystems, the only remaining interface belongs to the mechanical pitch control system. This system receives inputs from the present state of the FSM and outputs direction and step count instructions to the stepper motor to achieve the proper pitch angle. The transmission and reception of data through input and output ports on the STM32 allows the FSM to act as a feedback loop. It constantly receives updated information, reacts accordingly, and delivers the appropriate control message to each subsystem.

Testing

Assembly and Commissioning

1. Foundation Installation:
    a. Attach the transition piece to the turbine tower with three bolts
    b. Feed wires through the tower
    c. Clamp the transition piece to the foundation top tube
    d. Insert plastic tubing for pump to the hole on the bucket lid
    e. Using magnetic level, ensure that the tower is plumb
    f. While keeping the system plumb, lower the foundation into the water and allow the system to sink into the sand as far as possible
    g. Use the pump to suction water out of the top and press down on the tower base to fully insert the foundation until the lid contacts the sand
    h. Remove plastic tubing
2. Turbine Side Electronics:
    a. Mount the PCB into the nacelle using four bolts to secure it in place
    b. Place RE-50 power and ground wires in PCB terminals and screw into place for a secure connection
    c. Place the four stepper motor control wires in their respective PCB terminals and screw into place for a secure connection
    d. Place STM32 onto PCB's pin headers such that it is powered from the board and has GPIO pin connections via the PCB traces
    e. Run the power and ground wires from the PCB to the PCC, and connect to it using the anderson powerpole (APP) connectors
3. Load Side Electronics:
    a. Run the power and ground wires from the PCC to the UCL terminals and screw into place for a secure connection
    b. Plug the UCL into the 120V AC available power source

Power Curve Performance Task

The final blade design, Blade Design 2, was chosen because it ultimately performed better based on the scoring for the Power Curve task than Blade Design 1. The blades cut-in at around 3.40 m/s giving the system enough time and power to pitch from the cut-in angle, at 30° from vertical, to the power angle, 0°. The system's maximum power value, at 11 m/s was 20.8 watts with Blade Design 2 as opposed to 17.6 watts with Blade Design 1.

Using the UCL to test various resistances at each wind speed using maximum power point tracking (MPPT) controls. The manual controls of the UCL were tested to create power curves and find the maximum power at each wind speed from 5 to 11 m/s by changing the resistance between 2 ohms and 14 ohms. In comparison, when tested with a single resistance of 10 ohms, the overall power production was significantly lower, especially at high wind speeds.

Safety Task

At speeds up to 16 m/s, the turbine was tested for safety task using only the pitching mechanism to rotate the blades from power angle to stall angle – approximately -10° from vertical. Using this method, the turbine slowed to 10% of rated RPM within 10 seconds of the safety button being pressed. This pitching mechanism was very quick; however, the team has some concerns about mechanical loading conditions resulting from this method. Full-scale turbines often avoid pitching to stall due to increased loading and unpredictability of the turbine rotor in this position. The team plans to test the final blade design with two Safety task approaches during further testing before competition. The first method is a

pitch-to-stall technique that would be useful at lower wind speeds where the blades are positioned at the power angle. The second technique is pitch-to-feather. The pitch-to-feather method would unload the turbine under high wind speeds, and would also be more useful in restarting the turbine since the system must initiate fewer steps to get back to the cut-in position.

In addition to the pitch control mechanism, the team also tested generator breaking as a Safety task mechanism. This method was tested at wind speeds up to 16 m/s and was successful in slowing down the turbine quickly. However, this mechanism cannot reliably slow the turbine down to the required 10% of the rated rpm, so it would be used in tandem with the pitch control system. The relay switch to enable/disable generator braking uses very little power; therefore, the turbine can restart without significant power from the turbine side by simply unlatching the relay.

Durability Task

To prepare for durability task, the team tested the turbine several times in the wind tunnel at wind speeds up to 22 m/s. This task is ultimately most demanding on the foundation structure of the turbine. With this in mind, the turbine assembly was tested a number of times in the wind tunnel on a fixed structure to ensure durability of the blades and new pitch control system. Once these components were validated at higher wind speeds, the foundation component was installed in a tank with water and sand heights equal to those specified for competition. As discussed above, several foundation concepts were tested – each with the goal of maintaining under 6 mm of deflection up to the maximum competition wind speed.

To control the loads experienced by the system during this test, blades were pitched to an angle of 45°. By rotating the blades out of the wind in tandem with applying a small resistance via the UCL, the turbine will avoid potential runaway scenarios. Additionally, the UCL was programmed not to allow the turbine to exceed 15V, eliminating the chance of control loss during competition.

Appendix

Table A1. Pitch control and hub weighted decision matrix

	Relative Score (1-10)	Weighted Score	Relative Score (1-10)	Weighted Score	Relative Score (1-10)	Weighted Score	Relative Score (1-10)	Weighted Score	Relative Score (1-10)	Weighted Score	Relative Score (1-10)	Weighted Score	Relative Score (1-10)	Weighted Score	Relative Score (1-10)	Weighted Score	Total Score	**Ranking**
Rotational to Translational (Baseplate)	**Simplicity (Number of Parts)**		**Backdrivability**		**Proof of Concept, Reference**		**Cost**		**Precision of System**		**System Size**		**Maintenance**		**Responsiveness**			
Score Weight	0.5		0.7		0.5		0.3		0.8		0.5		0.1		0.6			
Stepper Motor with Linkage	7	3.5	6	4.2	10	5	9	2.7	7	5.6	8	4	8	0.8	10	6	31.8	**1**
Dual Shafted Stepper Motor with Rack and Pinion	7	3.5	6	4.2	5	2.5	8	2.4	4	3.2	6	3	8	0.8	9	5.4	25	**3**
Two-way Hydraulic Pumping	7	3.5	10	7	5	2.5	3	0.9	8	6.4	3	1.5	3	0.3	3	1.8	23.9	**4**
Linear Actuator	10	5	3	2.1	10	5	5	1.5	7	5.6	8	4	8	0.8	6	3.6	27.6	**2**
Current System	1	0.5	10	7	8	4	5	1.5	10	8	1	0.5	3	0.3	8	4.8	26.6	N/A (not compatible

	Relative Score (1-10)	Weighted Score	Relative Score (1-10)	Weighted Score	Relative Score (1-10)	Weighted Score	Relative Score (1-10)	Weighted Score	Relative Score (1-10)	Weighted Score	Relative Score (1-10)	Weighted Score	Total Score	Ranking
Translational to Rotational (Hub)	**Complexity (Number of Parts)**		**Backdrivability**		**Proof of Concept, Reference**		**Cost**		**System Size**		**Blade Alignment Precision**			
Score Weight	0.5		0.7		0.5		0.3		0.5		0.9			
RC Pitching	3	1.5	5	3.5	9	4.5	7	2.1	6	3	9	8.1	22.7	**1**
Rack and Pinion	4	2	7	4.9	9	4.5	5	1.5	5	2.5	4	3.6	19	**2**

References

[1] E. Osei, R. Opoku, A. Sunnu, and M. Adaramola, “Development of High Performance Airfoils for Application in Small Wind Turbine Power Generation,” *Journal of Energy*, vol. 2020, pp. 1–9, Feb. 2020, doi: 10.1155/2020/9710189.
[2] “The Wind Prospector.” https://maps.nrel.gov/wind-prospector/?aL=nd5nDN%255Bv%255D%3Dt%26kWBYWk%255Bv%255D%3Dt%26kWBYWk%255Bd%255D%3D1&bL=clight&cE=0&lR=0&mC=29.192930577727758%2C-94.43572998046875&zL=9 (accessed Apr. 24, 2022).